Design of a Polymer–Carbon Nanohybrid Junction by Interface Modeling for Efficient Printed Transistors

Do Hwan Kim,[†,§,‡] Hyeon-Jin Shin,[⊥,§] Hyo Sug Lee,[∥] Jiyoul Lee,[†] Bang-Lin Lee,[†] Wi Hyoung Lee,[△] Jong-Hwa Lee,[▽] Kilwon Cho,[△] Woo-Jae Kim,[▽,*] Sang Yoon Lee,[†,*] Jae-Young Choi,[⊥,*] and Jong Min Kim[#]

[†]Display Device Laboratory, [⊥]Graphene Center, [∥]Computational Science Laboratory, and [#]Frontier Research Laboratory, Samsung Advanced Institute of Technology, Samsung Electronics, Yongin, Gyeonggi-do 446-712, Korea, [△]Department of Chemical Engineering, Pohang University of Science and Technology, Pohang, 790-784, Korea, and [▽]Department of Chemical and Environmental Engineering, Gachon University, Sungnam, 461-701, Korea [§]These authors equally contributed to this work. [‡]Present address: Department of Chemical Engineering, Stanford University, 381 North-South Mall, Stanford, California 94305-5025, United States.

ABSTRACT

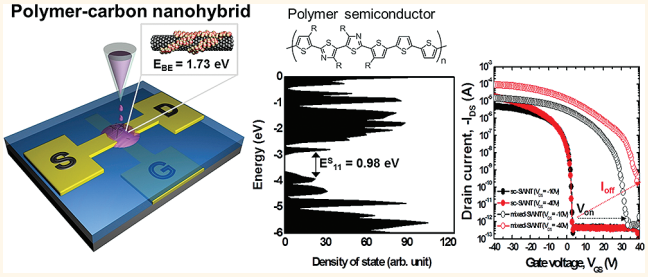

Molecularly hybridized materials composed of polymer semiconductors (PSCs) and single-walled carbon nanotubes (SWNTs) may provide a new way to exploit an advantageous combination of semiconductors, which yields electrical properties that are not available in a single-component system. We demonstrate for the first time high-performance inkjet-printed hybrid thin film transistors with an electrically engineered heterostructure by using specially designed PSCs and semiconducting SWNTs (sc-SWNTs) whose system achieved a high mobility of 0.23 $cm^2 V^{-1} s^{-1}$, no V_{on} shift, and a low off-current. PSCs were designed by calculation of the density of states of the backbone structure, which was related to charge transfer. The sc-SWNTs were prepared by a single cascade of the density-induced separation method. We also revealed that the binding energy between PSCs and sc-SWNTs was strongly affected by the side-chain length of PSCs, leading to the formation of a homogeneous nanohybrid film. The understanding of electrostatic interactions in the heterostructure and experimental results suggests criteria for the design of nanohybrid heterostructures.

KEYWORDS: polymer–carbon nanohybrid · printed transistors · electrostatic interaction · density of state · binding energy

Printable polymer semiconductors (PSCs) have attracted considerable attention because of their potential applications in large-area, low-cost, flexible, and printed optoelectronics.[1−4] However, the charge-carrier mobilities of PSC-based devices fabricated by inkjet printing are generally limited by hopping transport (lower conductivity) between polymer chains in disordered regions of such films. Therefore, the use of complementary heterostructures based on organic and inorganic semiconductors has been suggested as a potentially effective way to manipulate the optoelectronic properties of printed devices, as they may combine the desirable characteristics of both materials.[5−10] In particular, single-walled carbon nanotubes (SWNTs) have emerged as highly promising components of electronic and energy devices because of their high intrinsic charge-carrier mobility, high aspect ratio, and superior mechanical properties.[11−15] PSCs with SWNTs compose a promising heterostructure and were recently reported as a new platform for the next generation of optoelectronic devices, such as transistors,[16,17] photovoltaics,[18−20] photodetectors,[21] memories,[22] and sensors.[23]

Several groups have demonstrated that thin film transistors (TFTs) and photovoltaics with a PSC/SWNT heterostructure as the channel material have improved the charge-carrier mobility and on-current.[24−28] However, all approaches had a turn-on voltage (V_{on}) shift from the charge transfer between SWNTs and PSCs as well as a high off-current (I_{off}) because the pristine SWNTs had both semiconducting (sc-SWNTs) and metallic SWNTs (m-SWNTs). In a photovoltaic device, m-SWNT behavior in PSCs was discussed.[28] Furthermore, functionalized SWNTs and surfactants used for dispersion to make homogeneous nanohybrids impedes the molecular order and crystal structure of PSCs as well as the charge transfer between PSCs and SWNTs under an electrical bias, which has resulted in low-performance devices.[24,26,27] Although it was reported that specially designed PSCs selectively sorted sc-SWNTs[29,30] and the effect of SWNT chirality on the electrostatic interaction for the PSC/SWNT system[31,32] has been

* Address correspondence to wjkim@gachon.ac.kr; sangyoon.lee@samsung.com; jaeyoung88.choi@saumsung.com.

Received for review October 27, 2011 and accepted December 23, 2011.

Published online December 23, 2011
10.1021/nn2041472

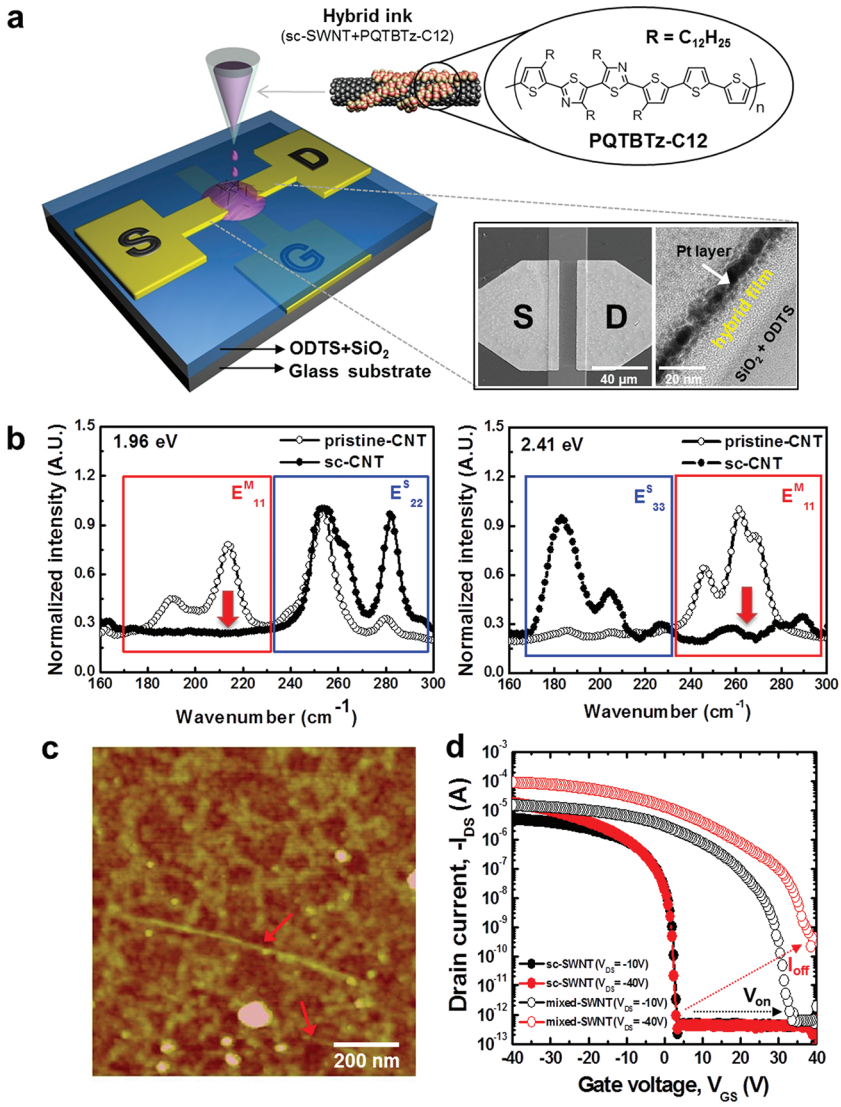

Figure 1. Printed nanohybrid semiconductors and transistor devices. (a) Schematic diagram of a back-gated and bottom-contact nanohybrid transistor built on well-dispersed PQTBTz-C12/SWNT ink using inkjet printing. Inset: Schematic picture of the PQTBTz-C12-wrapped SWNT and the morphological features of the TFT device fabricated by inkjet printing (plan image *via* FE-SEM and cross-sectional image *via* FE-TEM). (b) RBM regions in the Raman scattering spectra from the pristine [mixed metallic (m) and semiconducting (sc)]-SWNTs and the sc-SWNT using two excitation energies (1.96 and 2.41 eV). sc-SWNTs were prepared using a single cascade of the density-induced separation method. (c) Tapping-mode AFM height image of nanohybrid films printed on ODTS-modified SiO_2 surfaces. The annealing process was conducted at 180 °C. The red arrows show the sc-SWNTs dispersed in a PQTBTz-C12 matrix. (d) Transfer ($I_{DS}-V_{GS}$) characteristics of nanohybrid TFTs fabricated using the hybrid ink with pristine SWNTs (at 0.05 wt %) and the sc-SWNT (at 0.1 wt %) only. All samples were annealed at 180 °C under N_2 after the inkjet process and drying.

discerned, the electrical interaction mechanism between the PSCs and SWNTs in high-performance TFTs is not clearly understood. Therefore, it is crucial to understand the electrostatic interactions *via* charge transfer at the interface between the PSCs and SWNTs as well as to make well-dispersed sc-SWNTs in a PSC matrix for producing efficient, reliable nanohybrid semiconductor TFTs.

Herein, we suggest for the first time design criteria for PSC/SWNT nanohybrid semiconductors with an electrically engineered heterostructure for high-performance hybrid TFTs *via* inkjet printing. To understand the electrical interaction by charge transfer at the interface between the PSCs and SWNTs, we compared two types of printed TFTs, one with pristine (mixed m- and sc-) SWNTs and the other with sc-SWNTs. Furthermore, in this work, we used a new PSC, poly(didodecylquaterthiophene-*alt*-didodecylbithiazole) (PQTBTz-C12), which was designed to not only improve the molecular order of the polymer, as demonstrated in a previous study,[33] but also modulate the interaction with the sc-SWNTs without charge transfer. The sc-SWNT/PQTBTz-C12 nanohybrid system in this study provides a robust V_{on} with a high sc-SWNT concentration in a PQTBTz-C12 matrix, which is crucial for highly reliable printed TFTs. On the basis of our approach, we achieved a 3-fold higher mobility of 0.23 $cm^2\ V^{-1}\ s^{-1}$

compared with the pristine PQTBTz-C12. To further investigate the electrical interaction within the heterostructure, we determined the densities of states (DOS) and binding energies (E_{BE}) at the interface between the various PSCs and sc-SWNTs to discern the roles played by different PSC backbones and side-chain lengths. We were able to successfully incorporate PSCs/sc-SWNTs into a printed TFT, and we demonstrated that the heterostructures enhanced the mobility without a V_{on} shift.

RESULTS AND DISCUSSION

Figure 1a shows an overview of the printed nanohybrid semiconductors and transistor devices based on PQTBTz-C12 and the sc-SWNTs. We used the back-gated and bottom-contact transistor geometry (see Methods in Supporting Information for details). As the host PSC, we used the electron donor–acceptor PQTBTz-C12. Alkyl chain-substituted thiophene/thiazole blocks along the polymer backbone were assumed to increase the highest occupied molecular orbital level given the electron-accepting nature of the 5,5′-bithiazole units.[33] They also play roles as a semiconducting material and a dispersant, which could wrap the sc-SWNTs, as reported in other studies.[29−31] To decrease the strong interaction between the m-SWNTs and PSCs, the m-SWNTs were removed from the pristine SWNTs using a single cascade of the density-induced separation method (Figure S1, Supporting Information).[34,35] The radial breathing mode (RBM) for the Raman spectra of pristine SWNTs and sc-SWNTs at excitation energies 1.96 and 2.41 eV indicates that the m-SWNTs were clearly removed after separation (Figure 1b). This was also confirmed by the UV–vis–nIR absorption spectra (Figure S2, Supporting Information). To prepare the nanohybrid ink for the channel material in the TFTs, the separated sc-SWNTs and PQTBTz-C12 were formulated using a general dispersion method without additional dispersant. As shown in Figure 1c, an atomic force microscopy (AFM) image of the film printed using nanohybrid ink demonstrates that the sc-SWNTs (red arrows) were individually dispersed in the PQTBTz-C12 matrix. Figure 1d shows the transfer characteristics (I_{DS}–V_{GS}) of TFTs fabricated by two types of printed nanohybrids, one with pristine SWNTs at 0.05 wt % and the other with sc-SWNTs at 0.1 wt %. This indicates that SWNT chirality has a tremendous effect on device performance, such as V_{on}, I_{off}, and charge-carrier mobility (μ). TFTs with PQTBTz-C12/pristine SWNTs (0.42 $cm^2\ V^{-1}\ s^{-1}$) have a 2-fold higher charge-carrier mobility compared with PQTBTz-C12/sc-SWNTs (0.23 $cm^2\ V^{-1}\ s^{-1}$); however, I_{off} was increased by 2 orders of magnitude (10^{-10}A) in the saturation mode ($V_{DS} = -40$ V). More importantly, for PQTBTz-C12 with pristine SWNTs, V_{on} was shifted in the positive direction (35 V for the scan at $V_{DS} = -10$ V and above 40 V for the scan at $V_{DS} = -40$ V). This shift is

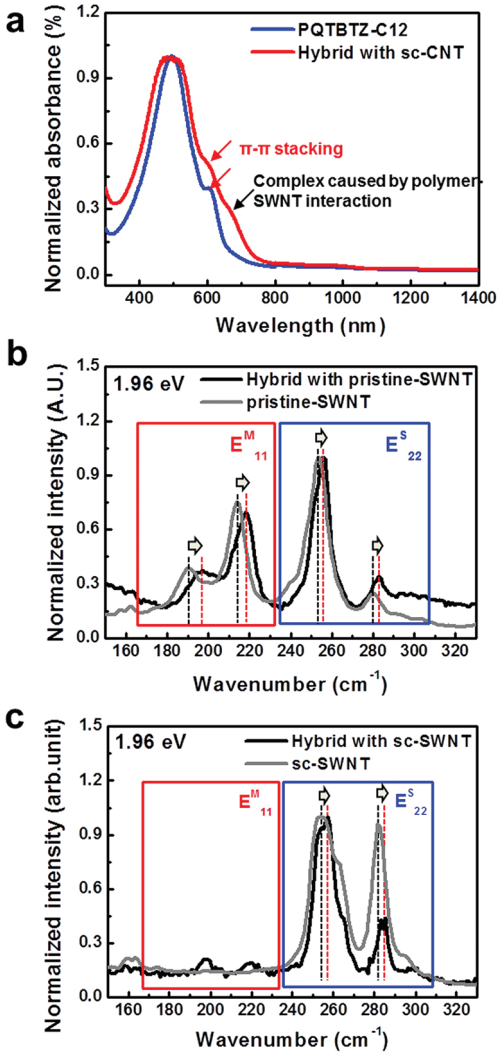

Figure 2. Interaction of SWNTs and PQTBTz-C12 in nanohybrids. (a) UV–vis absorption spectra of a PQTBTz-C12 solution at 0.1 wt % (in *ortho*-dichlorobenzene, ODCB) and a hybrid solution (at a total 0.1 wt % in ODCB) with 10% (w/w) sc-SWNTs to PQTBTz-C12. (b and c) Radial breathing modes (RBMs) measured at an excitation energy of 633 nm (1.96 eV) for the nanohybrid films with pristine- and sc-SWNTs, respectively. The arrows in (b) indicate a charge transfer between PQTBTz-C12 and the SWNTs.

attributed to the extra hole charges in the channel that were generated by a strong electrostatic interaction, even though an external bias was not applied. Recent studies have shown that the dominant presence of either metallic or small band gap semiconducting tubes might provide a sizable built-in potential at the interface for the holes to drift away.[31,36] Therefore, for a mixed distribution of semiconducting and metallic tubes, it is likely that the m-SWNTs have stronger interactions with PQTBTz-C12 because of the stronger electrostatic interaction due to the charge transfer, which generates a V_{on} shift in the positive direction and a high I_{off} in hybrid TFTs even at low SWNT loading. With a larger electron affinity than the PSCs, SWNTs serve as electron traps that affect the total charge density in the

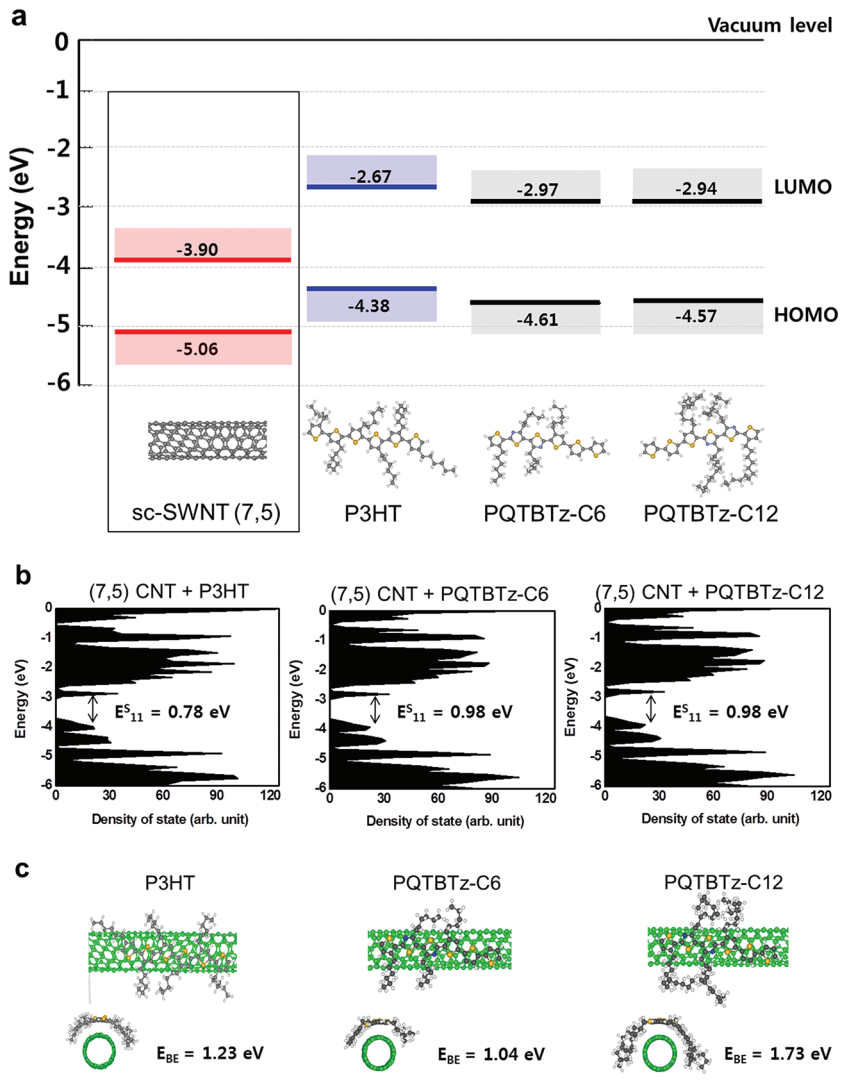

Figure 3. Molecular simulation of a nanohybrid semiconductor with (7,5) sc-SWNT heterostructures and polymer semiconductors. (a) Calculated electronic energy levels of sc-SWNTs and PSCs. The inset image shows (7,5) SWNT, P3HT with 6-mer thiophene oligomer, and PQTBTz-C6 and PQTBTz-C12 with six five-membered rings. (b) The density of states was calculated using the DFT method. The optimized model structure of the (7,5) sc-CNT and PSCs and their densities of states. (c) Longitudinal and radial schematic views of the nanohybrids with specific binding energies, depending on the PSC type. The binding energies (E_{BE}) were calculated using the minimized energy for each structure, E_{BE}[(7,5) SWNT/PSC] = E[(7,5) SWNT/PSC] − E[(7,5) SWNT] − E[PSC]. PSCs with a longer side chain interact more effectively with SWNTs.

ground state. Generally, the threshold voltage (V_{th}) for TFTs is proportional to the sum of the initial carrier density (n_0) and initial trapped carrier density (n_t) in the active layer,[26] as shown below.

$$V_{th} = -\frac{qh(n_0 + n_t)}{C_i}$$

q is the charge, h is the semiconductor film thickness, and C_i is the insulator capacitance per unit area. This implies that the reduction of the initial trapped charges *via* molecularly engineered PSCs and the separation of the sc-SWNTs are crucial for reliability in nanohybrid TFTs.

In nanohybrid ink, the dispersion of SWNTs has a strong effect on the optical and electrical characteristics.[37] Figure 2 shows the intermolecular interaction between the SWNTs and PQTBTz-C12 in the solution and in the solid states of a nanohybrid. A PSC solution composed of a 0.1 wt % PQTBTz-C12 (in *ortho*-dichlorobenzene, ODCB) and a nanohybrid solution (total 0.1 wt % PQTBTz-C12 in ODCB) with 10% (w/w) sc-SWNTs to PQTBTz-C12 was characterized using UV−vis−nIR absorption. A new peak near 670 nm was generated by the PQTBTz-C12 and sc-SWNT interaction, which is evidence for a well-dispersed nanohybrid solution (Figure 2a). It has been established that $\pi-\pi$ interactions between PSCs and SWNTs typically result in a band shift or broadening of the absorption peaks due to the change in the effective conjugation length of the PSCs with SWNTs.[38] To further clarify the interaction between the SWNTs and PQTBTz-C12 in the solid state by filtration of nanohybrid ink, the radial breathing modes in Raman scattering were characterized

at an excitation energy of 1.96 eV (Renishaw, RM-1000 Invia, 633 nm, He−Ne laser, 1800 L/mm grating, 0.7 cm^{-1} resolution). To investigate the effect of SWNT chirality on the intermolecular interactions, we prepared two types of nanohybrid film using pristine SWNTs (Figure 2b) and sc-SWNTs (Figure 2c) in PQTBTz-C12. The peaks in the red box originated from m-SWNT, and those in the blue box originated from sc-SWNT. Surprisingly, for the nanohybrid with pristine SWNTs, the peaks assigned in E^{M}_{11} are shifted up by ∼5−6 cm^{-1} compared with the pristine SWNTs. This shift can be ascribed to hardened and stiff C−C bonds,[39−42] which might be evidence of a strong electrostatic interaction at the interface of the PQTBTz-C12 backbone and the m-SWNTs. However, the peaks in the E^{S}_{22} (Figure 2b and c) were shifted up by only 2 cm^{-1} (not a notable change). This implies that the m-SWNTs can strongly withdraw an electron from the PQTBTz-C12 polymer backbone, compared with sc-SWNTs, because of a higher electron affinity, which leads to a charge transfer even at the ground state. As a result, when designing electrically engineered heterostructures at the ground state, it is essential to incorporate sc-SWNTs with PSCs, which can improve the reliability of TFT devices, as mentioned in Figure 1d.

However, even though sc-SWNTs are used, the type of PSC with the sc-SWNTs can have a tremendous effect on charge transfer in the heterostructures. To clarify this observation, we conducted a molecular simulation of the nanohybrids. A detailed atomic scheme of the electronic structure at the heterojunction may provide important insights into the existing experimental observations, which are not fully understood in detail. To further investigate the electrostatic interactions of the heterostructure, first-principles calculations based on the density functional theory (DFT), including van der Waals interactions,[43−47] were employed to investigate the nanohybrids with heterostructures for (7,5) sc-SWNT and PSCs as well as assess the effect of the PSC structure [(1) polymer backbone, (2) side-chain length] on charge transfer and binding energy in the nanohybrid. For the sc-SWNT, a (7,5) tube was used to represent the typical ∼0.8 nm diameter tube that dominantly existed in our experiment (Figure S2, Supporting Information).[48] For the PSCs, poly(hexylquaterthiophene-*alt*-dihexylbithiazole) (PQTBTz-C6) and PQTBTz-C12 were selected for an examination of how nanohybrids with different polymer structures affect the charge transfer and binding energies between PSCs and sc-SWNTs compared with poly-3-hexylthiophene (P3HT). The electronic energy levels for these materials are shown in Figure 3a. The highest occupied molecular orbital (HOMO)/lowest unoccupied molecular orbital (LUMO) levels for a single strand of semiconducting (7,5) SWNT and P3HT were calculated to be −5.06/−3.90 eV and −4.38/−2.67 eV, respectively, from the local vacuum level. The LUMO level of (7,5) SWNT is lower than P3HT with a difference of 1.23 eV. The LUMO levels of PQTBTz-C6 (−2.97 eV) and -C12 (−2.94 eV) are in close proximity to (7,5) SWNT compared with P3HT because of the electron-accepting thiazole moieties.[33] The electronic structure of PQTBTz, which has a band gap similar to P3HT, is precisely modulated to sc-SWNT after energy alignment with respect to (7,5) SWNT, which leads to a lower built-in potential compared with that of P3HT. Therefore, the electron transfer from PQTBTz to (7,5) SWNT in the ground state is expected to be reduced compared to P3HT, which results in an electrically stable heterostructure either without hole charge generation or with a lower charge. However, the SWNT Fermi level was suggested to be blue-shifted compared with the contacting P3HT, which behaves similar to a previous report.[18,31] This shift results in a large built-in potential; thus, this potential was attributed to a ground-state charge transfer from the P3HT backbone to the SWNT. To generate a change in energy state for the (7,5) SWNT as a function of the type of PSC, the density of states near the Fermi level for the nanohybrids and their optimized model structures were calculated using DFT, as shown in Figure 3b. For the (7,5) SWNT/P3HT heterojunction, the transition energy E^{S}_{11} was decreased to 0.78 eV (Figure 3b left) from 1.16 eV of (7,5) SWNT (Figure S3, Supporting Information), which is attributed to the change in the work function with respect to charge transfer.[49] In the (7,5) SWNT/PQTBTz-C6 and -C12 heterojunctions, however, the E^{S}_{11} near 0.98 eV is relatively similar to (7,5) SWNT (Figure 3b middle and right). Interestingly, there was small change in the E^{S}_{11} before and after energy alignment in the PQTBTz backbone system irrespective of side-chain length. This result implies that the PSC backbone structure primarily influences DOS structure. Furthermore, the binding energy between the (7,5) SWNT and PSCs, E_{BE} [(7,5) SWNT/PSC], strongly affects the dispersion of SWNTs in PSCs, which was estimated using the total energy difference between the bound and separated systems, E_{BE}[(7,5) SWNT/PSC] = E[(7,5) SWNT/PSC] − E[(7,5) SWNT] − E[PSC], as shown in Figure 3c. In this calculation, using semiempirical corrections, the van der Waals force is the primary interaction.[50] For PQTBTz-C6 and P3HT with a hexyl group side chain, the E_{BE}[(7,5) SWNT/PQTBTz-C6] of 1.04 eV is smaller than the E_{BE}[(7,5) SWNT/P3HT] of 1.23 eV for the rigid backbone of PQTBTz-C6 (Figure 3c). However, as side-chain length increases from a hexyl to dodecyl group, the E_{BE}[(7,5) SWNT/PQTBTz-C12] increases by 1.73 eV, which suggests that PSCs with a longer side chains can more effectively interact with SWNTs. On the basis of these results, we can conclude that the PSC side chains play a role in the formation of a well-defined nanohybrid by facilitating effective SWNT binding without a change in the DOS energy state. Therefore, these observations indicate that the roles of the PSC backbone and side chains can be divided in the heterostructures' electric interactions. Using nanohybrids with optimized PSCs,

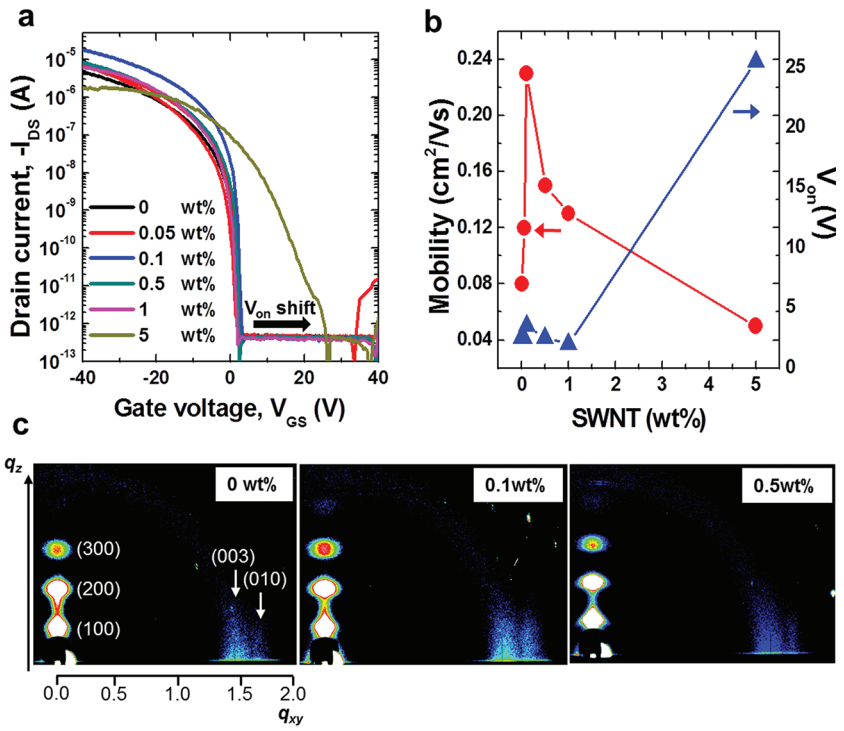

Figure 4. TFT performance as a function of sc-SWNT concentration and the corresponding crystalline microstructure in printed nanohybrid semiconductors. (a) Transfer characteristics of nanohybrid TFTs composed of PQTBTZ-C12 and sc-SWNTs, which show electrically stable heterostructures after incorporation of sc-SWNTs at 1 wt %. (b) Mobility and V_{on} plot as a function of sc-SWNT concentration. (c) 2D GIXD patterns for nanohybrid films that were inkjet printed onto ODTS-treated SiO_2 substrates as a function of SWNT concentration. The data are plotted *versus* the scattering vector, q, and the crystallographic assignments of the peaks are labeled. Most of the (h00) planes for the PQTBTz-C12 chains were oriented parallel to the gate dielectric (in the edge-on orientation) irrespective of the sc-SWNT concentration. Two intense in-plane reflections appeared vertically at a specific q_{xy} (>0), which were indexed to (003) and (010). The incident-beam angle was 0.3° to increase the scattering intensity.

the PQTBTz-C12 with an electrically stable energy state and physically strong binding energy has the most effective heterostructure, which considers the DOS and binding energy.

As already shown in Figure 1d, it is crucial to reduce the initial trapped charges for electrically stable printed hybrid TFTs. Even though we designed a PSC with optimized charge transfer and binding energy with respect to the sc-SWNTs, the effect of the sc-SWNT concentration on the initial trapped charges and charge-carrier mobilities (μ) should also be considered. Figure 4a shows the transfer characteristics (I_{DS}–V_{GS}) at the drain voltage (V_D = −40 V) of the printed hybrid TFTs with PQTBTz-C12 and various levels of sc-SWNTs, which ranged from 0.05 to 5 wt %. The μ were calculated in the saturation regime (V_{DS} = −40 V). Nanohybrid TFTs show higher μ (0.12−0.23 $cm^2\ V^{-1}\ s^{-1}$) than the pristine system (0.08 $cm^2\ V^{-1}\ s^{-1}$), except for PQTBTz-C12 with sc-SWNTs of 5 wt % (0.05 $cm^2\ V^{-1}\ s^{-1}$). In particular, hybrid devices exhibit the optimized characteristic for sc-SWNTs of 0.1 wt %, which will be discussed later. Furthermore, Figure 4b shows the relationship between V_{on} and the concentration of sc-SWNTs in hybrid TFTs. V_{on} is not changed by adding sc-SWNTs of up to 1 wt %, which indicates that extra hole charges *via* charge transfer from PQTBTz-C12 to sc-SWNTs were not generated. No distinguishable hysteresis was shown for all TFT devices (Figure S9, Supporting Information). This result is in contrast to other reports,[26,27] which show a significant V_{on} change even with SWNTs of 0.5 wt %. In brief, we can explain the charge-transporting mechanism under gate and drain bias as follows: The hole charges injected from the source electrode (Au) can move into the PQTBTz-C12 matrix. After that, hole charges are transferred to sc-SWNTs *via* hopping. At this moment, the energy level (HOMO) of polymer semiconductors is crucial for desired charge transfer. On the basis of Figure 3a, showing the energy diagram, the HOMO levels of PQTBTz-C6 (−4.61 eV) and -C12 (−4.57 eV) are in close proximity to the valence band (−5.06 eV) of sc-SWNT compared to P3HT (−4.38 eV). Therefore, the hole transfer from PQTBTz to sc-SWNT under gate and drain bias can be expected to be more efficient compared to P3HT. The hole charges reaching the interface of sc-SWNTs and PQTBTz-C12 can move to the PQTBTz-C12 matrix without barrier and finally reach the other electrode (drain). For PQTBTz-C12 with sc-SWNTs of 5 wt %, V_{on} was dramatically shifted in the positive direction (25.5 V), which might be attributed to trapped

hole charges at the grain boundary that are generated by a macrophase separation of PQTBTz-C12 and sc-SWNTs (Figure S4, Supporting Information). Also, in order to confirm the trend of V_{on} shift, we prepared hybrid TFT devices based on printed films with sc-SWNTs of 7 or 10 wt %. However, we could not address hybrid ink in the patterned channel region due to the strong charging effect of inks. This result implies that inducing a hybrid film with well-dispersed sc-SWNTs, which leads to an optimal blended ratio of sc-SWNTs, is required to avoid trapped charges in electrically engineered heterostructures.

To demonstrate the mechanism for enhanced hybrid TFT performance, we confirmed the effect on the crystalline microstructure (including molecular orientation and crystallinity) and optical behavior for the PQTBTz-C12/sc-SWNTs nanohybrids as a function of sc-SWNT concentration. To discern these effects, we used two-dimensional (2D) grazing incidence angle X-ray diffraction (GIXD), high-resolution X-ray diffraction, and UV−vis absorption spectroscopy, respectively. In Figure 4c, intense (*h*00) crystal reflections with higher order peaks, which could be used as a criterion for stacking due to the alkyl side chains along the *a*-axis, were found along the Debye rings in the q_z (out-of-plane) positions that satisfy Bragg's law. This result suggests that most of the (*h*00) planes in the PQTBTz-C12 chains were oriented parallel to the gate dielectric (in the edge-on orientation), irrespective of the level of sc-SWNTs, which coincides with high-resolution X-ray patterns (Figure S5, Supporting Information). Surprisingly, even with the inkjet-printed system, two intense rod-shaped in-plane reflections appeared vertically at a specific q_{xy} (>0), which were indexed to (003) and (010), indicating that the printed films consisted of multi-stacked layers preferentially oriented normal to the substrate in the lateral direction (Figure 4c). This result implies that hybrid films with sc-SWNTs of 0.1 and 0.5 wt % exhibit a more distinct rod of the (010) peak than the pristine film (Figure S6, Supporting Information), which is attributed to enhanced $\pi-\pi$ stacking of PQTBTz-C12 chains by SWNTs. This enhancement of $\pi-\pi$ stacking by mediating the crystallization of PQTBTz-C12 chains on the SWNT surface enables higher electrical performance for hybrid TFTs.[18] Furthermore, the UV−vis absorption behavior of the nanohybrid film is similar to 2D GIXD (Figure S7, Supporting Information). The intensity of the 599 nm shoulder peak due to $\pi-\pi$ stacking was increased when the sc-SWNTs were incorporated at 1 wt %; however, above 5 wt %, the intensity decreased (Figure S8, Supporting Information), which might be attributed to less ordering by macrophase separation, as shown in Figure S4 (Supporting Information). Hybrids with sc-SWNTs at 5 and 10 wt % have a blue-shifted absorption due to distortion of the PQTBTz-C12 backbones. In particular, the hybrid with sc-SWNTs of 10 wt % displays a strong blue-shifted absorption of 5 wt % due to aggregation as well as distortion of the polymer backbones, which might lead to more trap sites of charges. This result indicates that it is crucial to reduce the initial trapped charges using a homogeneous heterostructure for electrically reliable printed hybrid TFTs. Therefore, a well-dispersed sc-SWNT hybrid film can enhance the $\pi-\pi$ stacking of PQTBTz-C12 due to surface-induced crystallization at the SWNT wall surfaces, which leads to a high μ and no V_{on} shift in hybrid TFTs.

CONCLUSION

We have developed general criteria to control the μ, V_{on}, and I_{off} device properties in nanohybrid TFTs using an electrically engineered PSC and SWNT heterostructure. The m-SWNT had strong interactions with the PSCs, which resulted in a charge transfer and is attributed to a shifted V_{on} and increased I_{off}. The sc-SWNT/PQTBTz-C12 nanohybrid system has the advantages of a robust V_{on} even though sc-SWNT concentration increases in the PQTBTz-C12 matrix, which is crucial for high-quality TFTs. The species of SWNTs and homogeneity are key factors in controlling the V_{on} and I_{off}. Thus, printed TFTs with well-dispersed sc-SWNTs at 0.1 wt % in PQTBTz-C12 show three times higher μ (0.23 $cm^2\ V^{-1}\ s^{-1}$) than PSCs (0.08 $cm^2\ V^{-1}\ s^{-1}$) only. We also monitored the density of states and binding energies between the (7,5) sc-SWNT and diverse PSCs using first-principles calculations that were based on DFT. DOS was related to charge transfer and influenced by the PSC backbone structure, and the E_{BE} for the dispersion of SWNTs in PSCs was controlled by the side-chain length and did not affect the DOS. These results suggest criteria for the design of nanohybrid heterostructures. We believe that our approach will enable nanohybrid heterostructures to be utilized not only in printed TFTs but also in many practical optoelectronic devices.

EXPERIMENTAL SECTION

Separation and Purification of the SWNTs. As-prepared HiPco (purchased from Unidym) SWNTs were used for functionalization and separation. The SWNTs were dispersed in an H_2O solution with a 2% (w/v) sodium cholate surfactant (bile salts, Sigma-Aldrich) and sonicated (Sonics, Ultrasonic Processor: VCX-750), which was followed by ultracentrifugation (Beckman-Coulter, Ultracentrifuge: Optima L-100 XP) to remove SWNT bundles and other impurities. The resulting solution contained individually suspended SWNTs at a final concentration of 0.005% (w/v). A 4-nitrobenzene diazonium salt was used as a reagent to attach 4-nitrophenyl chemical handles onto m-SWNTs for separation, and the reaction was performed at 45 °C and pH 5.5, similar to a

previously reported method.[34] The separation of sc-SWNTs from m-SWNTs by density was performed using a density gradient method as reported previously[35] (see Supporting Information S1 for a more detailed separation mechanism). A density gradient was created using the nonionic medium iodixanol (OptiPrep, 60% (w/v) iodixanol, Sigma-Aldrich). The concentration of the initial gradient was adjusted to 30% (w/v) at 7 mL and was positioned at the top of a 60% (w/v) 3 mL stop-layer solution. The rest of the tube was filled with functionalized SWNT solutions of 5 mL. The sample was then centrifuged for 12 h at 22 °C and 32 000 rpm using a swinging-bucket rotor (Beckman Coulter, SW 32.1 Ti). The surfactant concentration was maintained at 2% (w/v) throughout the tube. The SWNT samples were fractionated at every 300 μL after centrifugation using a fraction recovery system (Beckman Coulter) and characterized by UV−vis−nIR absorption (Perkin-Elmer, Lambda750 UV−vis spectrometer) and Raman spectroscopy (Kaiser Raman RXN1 analyzer).

Preparation of the Hybrid ink. Poly(didodecylquaterthiophene-*alt*-didodecylbithiazole), PQTBTz-C12 (molecular weight, MW: 22 kDa), was synthesized as previously reported.[33] In a typical dispersion experiment, 0.1 mg of as-separated sc-SWNTs and 10 mg of PQTBTz-C12 were suspended in 10 mL of *ortho*-dichlorobenzene (purchased from Aldrich). The mixture was sonicated in a bath-type sonicator (Bandelin Electronic GMBH & Co. KG, Sonorex Super: RK106) for 10 h. To control the level of sc-SWNTs in the hybrid ink, the mixture solution was diluted without centrifugation into a PQTBTz-C12 solution with an alternative composition.

Computer Modeling. The first-principles calculations based on the density functional theory were performed using the VASP code to estimate the binding energies of the sc-CNT and polymers.[43−47] Supercells that included 244 carbon atom sites were used for the (7,5) sc-CNT. The cell length was 3.34 nm. The polymers were modeled with the 6-mer oligomers. The P3HT was modeled using 6-mer thiophenes, and the PQTBTz was modeled with the two thiazole units and four thiophene units. The plane-wave cutoff energy was 400 eV, and the gamma point calculations were performed. The exchange−correlation interactions between electrons were described using the generalized gradient approximation, and the projector-augmented wave potentials were used to describe ion−electron interactions.[51] We used the conjugate gradient method for geometry optimization, and the optimization procedure was truncated when the residual forces for the relaxed atoms were less than 0.03 eV/Å.

The binding energies were calculated using the total energy differences between the bound and separated systems, $E_{BE}(AB) = E(AB) - E(A) - E(B)$. For this calculation using the DFT-D2 method with semiempirical corrections, the van der Waals interaction was shown to be the primary interaction.[51]

Characterization of the Films. To confirm the nanomorphology and crystalline microstructure, the PQTBTz-C12 and hybrid thin films with SWNTs were ink-printed from 0.2 wt % solutions in *ortho*-dichlorobenzene on ODTS-treated SiO_2 substrates and annealed at 180 °C for 1 h under N_2. An atomic force microscope (Dimension V, Veeco Co.) operating in the tapping mode with a carbon nanotube cantilever was used to characterize the surface morphologies of the samples. High-resolution field-emission transmission electron microscopy (HR-TEM, JEM 2100F, JEOL) with a 120 kV accelerating voltage was used to characterize nanohybrid film thickness in the TFT device. Raman spectroscopy (Renishaw, RM-1000 Invia, 514 nm, Ar+ ion laser, 2400 L/mm grating, 0.7 cm^{-1} resolution) was used to classify m-SWNTs and sc-SWNTs. The grazing-incidence X-ray diffraction and high-resolution X-ray diffraction measurements were performed at the 4C2 and 10C1 beamline (wavelength ~1.54 Å) in the Pohang Accelerator Laboratory. The UV−vis measurements were performed using a UV−vis−near IR spectrophotometer (Varian, Cary-5000).

Fabrication of the Thin Film Transistor. We used the back-gated and bottom-contact transistor geometry with 3-mercaptopropyl triethoxysilane/Au (8 Å/70 nm) source (S)/drain (D) contacts and a SiO_2 (300 nm) gate dielectric that was modified with octadecyltrichlorosilane (ODTS). The hybrid thin films with PQTBTz-C12/SWNTs were inkjet printed from a 0.2 wt % solution in *ortho*-dichlorobenzene on ODTS-treated SiO_2 substrates and annealed at 180 °C for 1 h under N_2. The standard channel length and width were 12 and 120 μm, respectively. A Keithley 4200-SCS semiconductor parameter analyzer was used to conduct all of the measurements for the current−voltage characteristics under ambient condition and N_2.

Acknowledgment. We gratefully acknowledge helpful technical support of atomic force microscopy by Ms. Y. Kwon and field-emission transmission electron microscopy by Mr. I. Y. Song in the AE group at SAIT and the Pohang Accelerator Laboratory for providing the 4C2 and 10C1 beamlines used in this study. This work was supported by the Basic Science Research Program through the National Research Foundation of Korea (NRF) funded by the Ministry of Education, Science and Technology (2011-0005392), and the Human Resources Development of the Korea Institute of Energy Technology Evaluation Planning (KETEP) grant funded by the Korea Government Ministry of Knowledge Economy (No. 20104010100510).

Supporting Information Available: Additional figures. This material is available free of charge *via* the Internet at http://pubs.acs.org.

REFERENCES AND NOTES

1. Katz, H. E.; Bao, Z.; Gilat, S. L. Synthetic Chemistry for Ultrapure, Processable, and High-Mobility Organic Transistor Semiconductors. *Acc. Chem. Res.* **2001**, *34*, 359–369.
2. Dimitrakopoulos, C. D.; Malenfant, P. R. L. Organic Thin Film Transistors for Large Area Electronics. *Adv. Mater.* **2002**, *14*, 99–117.
3. Sirringhaus, H.; Brown, P. J.; Friend, R. H.; Nielsen, M. M.; Bechgaard, K.; Langeveld-Voss, B. M. W.; Spiering, A. J. H.; Janssen, R. A. J.; Meijer, E. W.; Herwig, P.; *et al*. Two-Dimensional Charge Transport in Self-Organized, High-Mobility Conjugated Polymers. *Nature* **1999**, *401*, 685–688.
4. McCulloch, I.; Heeney, M.; Bailey, C.; Genevicius, K.; MacDonald, I.; Shkunov, M.; Sparrowe, D.; Tierney, S.; Wagner, R.; Zhang, W.; *et al*. Liquid-Crystalline Semiconducting Polymers with High Charge-Carrier Mobility. *Nat. Mater.* **2006**, *5*, 328–333.
5. Kagan, C. R.; Mitzi, D. B.; Dimitrakopoulos, C. D. Organic-Inorganic Hybrid Materials as Semiconducting Channels in Thin-Film Field-Effect Transistors. *Science* **1999**, *286*, 945–947.
6. Huynh, W. U.; Dittmer, J. J.; Alivisatos, A. P. Hybrid Nanorod-Polymer Polar Cells. *Science* **2002**, *295*, 2425–2427.
7. Singh, S. P.; Ooi, Z.-E.; Geok, S. N. L.; Goh, G. K. L.; Dodabalapur, A. Electrical Characteristics of Zinc Oxide-Organic Semiconductor Lateral Heterostructure Based Hybrid Field-Effect Bipolar Transistors. *Appl. Phys. Lett.* **2011**, *98*, 073302–073304.
8. Blumstengel, S.; Glowatzki, H.; Sadofev, S.; Koch, N.; Kowarik, S.; Rabe, J. P.; Henneberger, F. Band-Offset Engineering in Organic/Inorganic Semiconductor Hybrid Structures. *Phys. Chem. Chem. Phys.* **2010**, *12*, 11642–11646.
9. Sofos, M.; Goldberger, J.; Stone, D. A.; Allen, J. E.; Ma, Q.; Herman, D. J.; Tsai, W.-W.; Lauhon, L. J.; Stupp, S. I. A Synergistic Assembly of Nanoscale Lamellar Photoconductor Hybrids. *Nat. Mater.* **2009**, *8*, 68–75.
10. Liscio, A.; Veronese, G. P.; Treossi, E.; Suriano, F.; Rossella, F.; Bellani, V.; Rizzoli, R.; Samorì, P.; Palermo, V. Charge Transport in Graphene-Polythiophene Blends as Studied by Kelvin Probe Force Microscopy and Transistor Characterization. *J. Mater. Chem.* **2011**, *21*, 2924–2931.
11. Hu, L.; Hecht, D. S.; Grüner, G. Carbon Nanotube Thin Films: Fabrication, Properties, and Applications. *Chem. Rev.* **2010**, *110*, 5790–5844.
12. Kang, S. J.; Kocabas, C.; Ozel, T.; Shim, M.; Pimparkar, N.; Alam, M. A.; Rotkin, S. V.; Rogers, J. A. High-Performance Electronics using Dense, Perfectly Aligned Arrays of Single-Walled Carbon Nanotubes. *Nat. Nanotechnol.* **2007**, *2*, 230–236.
13. Snow, E. S.; Perkins, F. K.; Houser, E. J.; Badescu, S. C.; Reinecke, T. L. Chemical Detection with a Single-Walled

Carbon Nanotube Capacitor. *Science* **2005**, *307*, 1942–1945.
14. Sun, D.; Timmermans, M. Y.; Tian, Y.; Nasibulin, A. G.; Kauppinen, E. I.; Kishimoto, S.; Mizutani, T.; Ohno, Y. Flexible High-Performance Carbon Nanotubes Integrated Circuits. *Nat. Nanotechnol.* **2011**, *6*, 156–161.
15. LeMieux, M. C.; Roberts, M.; Barman, S.; Jin, Y. W.; Kim, J. M.; Bao, Z. Self-Sorted, Aligned Nanotube Networks for Thin-Film Transistors. *Science* **2008**, *321*, 101–104.
16. Harris, K. D.; Xiao, S.; Lee, C. Y.; Strano, M. S.; Nuckolls, C.; Blanchet, G. B. High Mobility, Air-Stable Organic Transistors from Hexabenzocoronene/Carbon Nanotube Bilayers. *J. Phys. Chem. C* **2007**, *111*, 17947–17951.
17. Kumar, S.; Blanchet, G. B.; Hybertsen, M. S.; Murthy, J. Y.; Alam, M. A. Performance of Carbon Nanotube-Dispersed Thin-Film Transistors. *Appl. Phys. Lett.* **2006**, *89*, 143501–143503.
18. Geng, J.; Zeng, T. Influence of Single-Walled Carbon Nanotubes Induced Crystallinity Enhancement and Morphology Change on Polymer Photovoltaic Devices. *J. Am. Chem. Soc.* **2006**, *128*, 16827–16833.
19. Holt, J. M.; Ferguson, A. J.; Kopidakis, N.; Larsen, B. A.; Bult, J.; Rumbles, G.; Blackburn, J. L. Prolonging Charge Separation in P3HT-SWNT Composites using Highly Enriched Semiconducting Nanotubes. *Nano Lett.* **2010**, *10*, 4627–4633.
20. Ferguson, A. J.; Blackburn, J. L.; Holt, J. M.; Kopidakis, N.; Tenent, R. C.; Barnes, T. M.; Heben, M. J.; Rumbles, G. Photo Induced Energy and Charge Transfer in P3HT:SWNT Composites. *J. Phys. Chem. Lett.* **2010**, *1*, 2406–2411.
21. Liao, S.-Y.; Maneux, C.; Pouget, V.; Fré gonè se, S.; Zimmer, T. Compact Modeling of Optically Gated Carbon Nanotube Field Effect Transistor. *Status Solidi B* **2010**, *247*, 1858–1861.
22. Borghetti, J.; Derycke, V.; Lenfant, S.; Chenevier, P.; Filoramo, A.; Goffman, M.; Vuillaume, D.; Bourgoin, J.-P. Optoelectronic Switch and Memory Devices Based on Polymer Functionalized Carbon Nanotube Transistors. *Adv. Mater.* **2006**, *18*, 2535–2540.
23. Wang, F.; Gu, H.; Swager, T. M. Carbon Nanotube/Polythiophene Chemiresistive Sensors for Chemical Warfare Agents. *J. Am. Chem. Soc.* **2008**, *130*, 5392–5393.
24. Park, Y. D.; Lima, J. A.; Jang, Y.; Hwang, M.; Lee, H. S.; Lee, D. H.; Lee, H.-J.; Baek, J.-B.; Cho, K. Enhancement of the Field-Effect Mobility of Poly(3-hexylthiophene)/Functionalized Carbon Nanotube Hybrid Transistors. *Org. Electron.* **2008**, *9*, 317–322.
25. Liu, S.; Mannsfeld, S. C. B.; LeMieux, M. C.; Lee, H. W.; Bao, Z. Organic Semiconductor-Carbon Nanotube Bundle Bilayer Field Effect Transistors with Enhanced Mobilities and High On/Off Ratios. *Appl. Phys. Lett.* **2008**, *92*, 053306–053308.
26. Tsukamoto, J.; Mata, J.; Matsuno, T. Organic Field Effect Transistors Using Composites of Semiconductive Polymers and Single-Walled Carbon Nanotubes. *Jpn. J. Appl. Phys.* **2007**, *46*, L396–L398.
27. Bo, X. Z.; Lee, C. Y.; Strano, M. S.; Goldfinger, M.; Nuckolls, C.; Blanchet, G. B. Carbon Nanotubes-Semiconductor Networks for Organic Electronics: The Pickup Stick Transistor. *Appl. Phys. Lett.* **2005**, *86*, 182102–182104.
28. Ham, M.-H.; Paulus, G. L. C.; Lee, C. Y.; Song, C.; Kalantarzadeh, K.; Choi, W.; Han, J.-H.; Strano, M. S. Evidence for High-Efficiency Exciton Dissociation at Polymer/Single-Walled Carbon Nanotube Interfaces in Planar Nano-heterojunction Photovoltaics. *ACS Nano* **2010**, *4*, 6251–6259.
29. Nish, A.; Hwang, J.-Y.; Doig, J.; Nicholas, R. J. Highly Selective Dispersion of Single Walled Carbon Nanotubes using Aromatic Polymers. *Nat. Nanotechnol.* **2007**, *2*, 640–646.
30. Ozawa, H.; Fujigaya, T.; Niidome, Y.; Hotta, N.; Fujiki, M.; Nakashima, N. Rational Concept To Recognize/Extract Single-Walled Carbon Nanotubes with a Specific Chirality. *J. Am. Chem. Soc.* **2011**, *133*, 2651–2657.
31. Kanai, Y.; Grossman, J. C. Role of Semiconducting and Metallic Tubes in P3HT/Carbon-Nanotube Photovoltaic Heterojunctions: Density Functional Theory Calculations. *Nano Lett.* **2008**, *8*, 908–912.
32. Lu, F.; Meziani, M. J.; Cao, L.; Sun, Y.-P. Separated Metallic and Semiconducting Single-Walled Carbon Nanotubes: Opportunities in Transparent Electrodes and Beyond. *Langmuir* **2011**, *27*, 4339–4350.
33. Kim, D. H.; Lee, B.-L.; Moon, H.; Kang, H. M.; Jeong, E. J.; Park, J.-I.; Han, K.-M.; Lee, S.; Yoo, B. W.; Koo, B. W.; *et al.* Liquid-Crystalline Semiconducting Copolymers with Intramolecular Donor-Acceptor Building Blocks for High-Stability Polymer Transistors. *J. Am. Chem. Soc.* **2009**, *131*, 6124–6132.
34. Kim, W.-J.; Usrey, M. L.; Strano, M. S. Selective Functionalization and Free Solution Electrophoresis of Single-Walled Carbon Nanotubes: Separate Enrichment of Metallic and Semiconducting SWNT. *Chem. Mater.* **2007**, *19*, 1571–1576.
35. Kim, W.-J.; Nair, N.; Lee, C. Y.; Strano, M. S. Covalent Functionalization of Single Walled Carbon Nanotubes Alters Their Densities Allowing Electronic and Other Types of Separation. *J. Phys. Chem. C* **2008**, *112*, 7326–7331.
36. Kymakis, E., Amaratunga, A. J. In *Organic PhotoVoltaics*; Sun, S.-S., Sariciftci, N. S., Eds.; CRC Press: Boca Raton, FL, 2005.
37. Wang, J.; Früchtl, D.; Sun, Z.; Coleman, J. N.; Blau, W. J. Control of Optical Limiting of Carbon Nanotube Dispersions by Changing Solvent Parameters. *J. Am. Chem. Soc.* **2010**, *114*, 6148–6156.
38. Star, A.; Stoddart, J. F.; Steuerman, D.; Diehl, M.; Boukai, A.; Wong, E. W.; Yang, X.; Chung, S.-W.; Choi, H.; Heath, J. R. Preparation and Properties of Polymer-Wrapped Single-Walled Carbon Nanotubes. *Angew. Chem., Int. Ed.* **2001**, *40*, 1721–1725.
39. Loi, M. A.; Gao, J.; Cordella, F.; Blondeau, P.; Menna, E.; Bártová, B.; Hébert, C.; Lazar, S.; Botton, G. A.; Milko, M.; *et al.* Encapsulation of Conjugated Oligomers in Single-Walled Carbon Nanotubes: Towards Nanohybrids for Photonic Devices. *Adv. Mater.* **2010**, *22*, 1635–1639.
40. Takenobu, T.; Takano, T.; Shiraishi, M.; Murakami, Y.; Ata, M.; Kataura, H.; Achiba, Y.; Iwasa, Y. Stable and Controlled Amphoteric Doping by Encapsulation of Organic Molecules inside Carbon Nanotubes. *Nat. Mater.* **2003**, *2*, 683–688.
41. Rucha, P. W.; Hardwick1, L. J.; Hahn, M.; Foelskea, A.; Kötz, R.; Wokauna, A. Electrochemical Doping of Single-Walled Carbon Nanotubes in Double Layer Capacitors Studied by *in Situ* Raman Spectroscopy. *Carbon.* **2009**, *47*, 38–52.
42. Farhat, H.; Sasaki, K.; Kalbac, M.; Hofmann, M.; Saito, R.; Dresselhaus, M. S.; Kong, J. Softening of the Radial Breathing Mode in Metallic Carbon Nanotubes. *Phys. Rev. Lett.* **2009**, *102*, 126804–126808.
43. Kresse, G.; Hafner, J. *Ab Initio* Molecular Dynamics for Liquid Metals. *Phys. Rev. B* **1993**, *47*, 558–561.
44. Kresse, G.; Hafner, J. *Ab Initio* Molecular-Dynamics Simulation of the Liquid-Metal−Amorphous-Semiconductor Transition in Germanium. *Phys. Rev. B* **1994**, *49*, 14251–14269.
45. Kresse, G.; Furthmüller, J. Efficiency of *ab-Initio* Total Energy Calculations for Metals and Semiconductors using a Plane-Wave Basis Set. *Comput. Mater. Sci.* **1996**, *6*, 15–50.
46. Kresse, G.; Furthmüller, J. Efficient Iterative Schemes for *ab Initio* Total-Energy Calculations using a Plane-Wave Basis Set. *Phys. Rev. B* **1996**, *54*, 11169–11186.
47. Blochl, P. E. Projector Augmented-Wave Method. *Phys. Rev. B* **1994**, *50*, 17953–17979.
48. Liu, H.; Nishide, D.; Tanaka, T.; Kataura, H. Large-Scale Single-Chirality Separation of Single-Wall Carbon Nanotubes by Simple Gel Chromatography. *Nat. Commun.* **2011**, *2*, 309.
49. Kim, K. K.; Bae, J. J.; Park, H. K.; Kim, S. M.; Geng, H. -Z.; Park, K. A.; Shin, H.-J.; Yoon, S.-M.; Benayad, A.; *et al.* Fermi Level Engineering of Single-Walled Carbon Nanotubes by $AuCl_3$ Doping. *J. Am. Chem. Soc.* **2008**, *130*, 12757–12761.
50. Grimme, S. Semiempirical GGA-Type Density Functional Constructed with a Long-Range Dispersion Correction. *Comput. Chem.* **2006**, *27*, 1787–1799.
51. Kresse, G.; Joubert, D. From Ultrasoft Pseudopotentials to the Projector Augmented-Wave Method. *Phys. Rev. B* **1999**, *59*, 1758–1775.